ORIGINAL PAPER

Extension of the open-source TIGRE toolbox for proton imaging

Stefanie Kaser [a,*], **Thomas Bergauer** [a], **Ander Biguri** [b], **Wolfgang Birkfellner** [c], **Sepideh Hatamikia** [d,e,c], **Albert Hirtl** [f], **Christian Irmler** [a], **Benjamin Kirchmayer** [f], **Felix Ulrich-Pur** [g,a]

[a] Institute of High Energy Physics, Austrian Academy of Sciences, Vienna, Austria
[b] Department of Applied Mathematics and Theoretical Physics (DAMTP), University of Cambridge, Cambridge, United Kingdom
[c] Center for Medical Physics and Biomedical Engineering, Medical University of Vienna, Vienna, Austria
[d] Austrian Center for Medical Innovation and Technology, Wiener Neustadt, Austria
[e] Research Center for Medical Image Analysis and Artificial Intelligence (MIAAI), Department of Medicine, Danube Private University, Krems, Austria
[f] Atominstitut, TU Wien, Vienna, Austria
[g] GSI Helmholtzzentrum für Schwerionenforschung GmbH, Darmstadt, Germany

Received 29 April 2022; accepted 31 August 2022

Abstract

Proton irradiation is a well-established method to treat deep-seated tumors in radio oncology. Usually, an X-ray computed tomography (CT) scan is used for treatment planning. Since proton therapy is based on the precise knowledge of the stopping power describing the energy loss of protons in the patient tissues, the Hounsfield units of the planning CT have to be converted. This conversion introduces range errors in the treatment plan, which could be reduced, if the stopping power values were extracted directly from an image obtained using protons instead of X-rays. Since protons are affected by multiple Coulomb scattering, reconstruction of the 3D stopping power map results in limited image quality if the curved proton path is not considered. This work presents a substantial code extension of the open-source toolbox TIGRE for proton CT (pCT) image reconstruction based on proton radiographs including a curved proton path estimate. The code extension and the reconstruction algorithms are GPU-based, allowing to achieve reconstruction results within minutes. The performance of the pCT code extension was tested with Monte Carlo simulated data using three phantoms (Catphan® high resolution and sensitometry modules and a CIRS patient phantom). In the simulations, ideal and non-ideal conditions for a pCT setup were assumed. The obtained mean absolute percentage error was found to be below 1% and up to 8 lp/cm could be resolved using an idealized setup. These findings demonstrate that the presented code extension to the TIGRE toolbox offers the possibility for other research groups to use a fast and accurate open-source pCT reconstruction.

Keywords: GPU-based imaging; Iterative image reconstruction; Proton computed tomography; Proton radiography

* Corresponding author.
E-mail: stefanie.kaser@oeaw.ac.at (S. Kaser).

Z Med Phys **xxx** (2022) xxx–xxx
https://doi.org/10.1016/j.zemedi.2022.08.005
www.elsevier.com/locate/zemedi

1 Introduction

In cancer therapy, proton beams have become a well-established method to irradiate deep-seated tumors. A planning CT is typically required prior to the treatment session. This CT is usually performed with X-rays, thus providing the linear attenuation coefficients in Hounsfield units. Since proton therapy is based on stopping power (SP) values describing the energy loss of a charged particle in the patient tissues, a conversion procedure is necessary [1]. This conversion leads to range uncertainties in the calculated dose distribution. Therefore, the idea of proton imaging, where the same particle is used for the planning CT and the subsequent irradiation treatment, was developed [2,3]. Using this approach, the relative stopping power (RSP), i.e. the SP expressed relative to the SP of water, can be obtained from the planning CT directly.

In contrast to photons, protons do not pass through the patient tissue on a straight-line path due to multiple Coulomb scattering (MCS). Therefore, their trajectory must be monitored during the CT measurement and later incorporated into the reconstruction process. To account for that, a potential proton CT (pCT) setup, as described in Schulte et al. [2], consists of four tracking planes: two upstream and two downstream of the object to be imaged (phantom). While an additional calorimeter allows measuring the residual particle energies (giving the projection value in proton radiography), the tracker planes are used to determine the position and direction of each particle prior to entering and after passing through the patient.

Multiple image reconstruction techniques, using direct [4,5] or iterative algorithms [6,7] were developed for pCT. Iterative reconstruction approaches are often based on accelerated implementations using graphics processing units (GPU) [6] since individual particle tracks have to be considered in the reconstruction process. Direct algorithms, on the other hand, profit from shorter reconstruction time in general. However, for X-ray CT scans, they are known for their lower reconstruction performance as compared to iterative reconstruction techniques for cases with limited and noisy input data [8]. For pCT, Hansen et al. [6] showed that direct and iterative algorithms yield comparable results in terms of spatial resolution and image quality when sinogram interpolation is used for the direct method, which prevents breaking down of the method at low imaging doses.

Recently, a simple pCT reconstruction approach [9] using the iterative algorithms implemented in an existing X-ray CT reconstruction toolkit, namely the Tomographic Iterative GPU-based REconstruction toolbox TIGRE [8], was published. Although the proposed method could demonstrate the advantages of the framework, it suffered from the simplified assumptions due to the straight-line approach initially implemented in the TIGRE toolbox. In the present work, as improvement of this initial reconstruction workflow, a newly written code extension for pCT image reconstruction for the TIGRE toolbox is presented. It allows calculating high resolution proton radiographs based on the maximum likelihood method described by Collins-Fekete et al. [10]. In their approach, which was slightly refined in this work, the projection data are binned in multiple channels using an optimized cubic spline [11]. The method presented in this work defines a channel as a three-dimensional extension of a detector pixel to the source position (see Fig. 1), allowing to generate radiographs containing the path information of single protons. Implementing the method into the TIGRE toolbox as a pre-reconstruction binning enables the use of the reconstruction algorithms already implemented for X-ray CT also for proton CT reconstruction without modification.

The performance of the new open-source code extension of the TIGRE toolbox is demonstrated by following two approaches: as a reference, the original methodology of the pre-reconstruction binning as described by Collins-Fekete et al. [10] was implemented and tested in TIGRE. This original implementation did not use a convex hull [12,13] in the binning process. Furthermore, a refinement of the method is demonstrated using pCT data obtained from Monte Carlo simulations. The refined approach uses a simplified object-surrounding hull model instead of the actual convex hull (see Section 2.3) and channel weighting (channels within the hull receive a higher weight than air channels). In contrast to Collins-Fekete et al. [10] and Khellaf et al. [5], where a filtered back-projection was used to reconstruct an RSP map from the radiographs, the iterative adaptive-steepest-descent projection onto convex sets (ASD-POCS) algorithm was used in this work for pCT reconstruction.

2 Materials and methods

2.1 Monte Carlo simulations

A pCT setup with four silicon tracking detectors in an air volume was simulated in Geant4 [14] version 10.5.1 using the physics list *QGSP_BIC*. The initial beam energy E_{init} was set to 200 MeV in all simulations. Detector distances are shown in Fig. 2. As in Kaser et al. [9], no additional calorimeter was simulated, but the energy was directly measured at the tracking planes. Two configurations were investigated:

- **Ideal setup:** To minimize the impact of the tracking system on the reconstruction result, a thickness of 1 μm was chosen for the tracking detectors. Ideal energy and spatial resolution of the detectors were assumed. The energy loss in the phantom was determined by calculating the difference of the proton energies at the upstream surfaces of detectors D2 and D3.

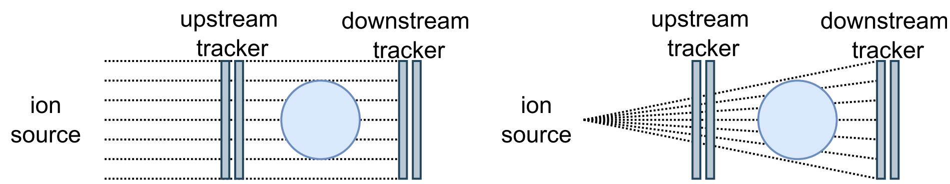

Figure 1. Sketch for the definition of channels [10] using a planar source (left) and a point source (right). The resulting channels are indicated as dotted black lines.

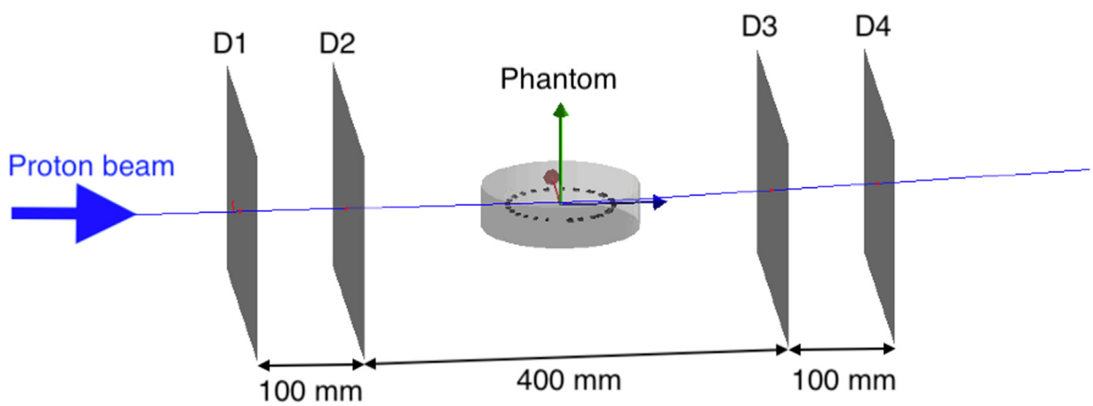

Figure 2. Sketch of the pCT setup used in the Monte Carlo simulations.

- **Non-ideal setup:** To investigate the performance of the reconstruction under more realistic conditions, the thickness per tracking detector was set to 300 μm. This corresponds to a typical size for double-sided silicon strip detectors, as for example used for a pCT demonstrator in Ulrich-Pur et al. [15]. The residual energy was measured at the upstream surface of detector D4 and subtracted from a fixed initial energy (average energy measured at the tracker plane directly upstream of the phantom, D2). A spatial resolution of $\sigma_s = 0.15$ mm (as in Khellaf et al. [5]) and an energy resolution of $\Delta E/E = 1\%$ were selected. These detector effects were applied prior to any further calculation, and hence affect the calculation of the particle directions and subsequently the proton path estimates. Note that these simulation parameters still do not represent a fully realistic pCT setup, however, they incorporate several general features as expected in real systems.

In both cases, the energy loss was converted to a water-equivalent path length (WEPL) using a fit obtained from a Geant4 [14] Monte Carlo simulation, where proton beams in the energy range from 20 MeV to 250 MeV were hitting a cuboid water absorber. The R80, i.e., the range in the water cube where the Bragg peak has decreased to 80% of its maximum, was fitted over the given energy range [16]. Subsequently, this fit could be used to determine the corresponding R80 in water of a specific proton energy. This calculation was performed for the residual and initial proton energy, which were obtained for each proton from the Geant4 simulations investigating a specific phantom (as described in the following paragraphs). Calculating the difference of the R80 obtained for initial and residual energy yielded the WEPL.

The Catphan® [17] modules high resolution (CTP528, The Phantom Laboratory Incorporated, Salem, NY, USA) and sensitometry (CTP404, The Phantom Laboratory Incorporated, Salem, NY, USA) were chosen as phantoms in this study and are schematically displayed in Fig. 3. Both modules have cylindrical bodies made from acrylic (diameter of 150mm) with specific inserts and a height of 40mm (high resolution) and 25mm (sensitometry). The high resolution module contains line pair inserts made from aluminum to determine the spatial resolution of a reconstruction, whereas the sensitometry module contains cylindrical inserts (diameter of 12.5mm) of various materials to analyze the RSP accuracy. Both phantoms are typically used to determine the quality of a reconstruction in ion imaging [4,18,19]. In the simulations, 225 protons per mm^2 (in the phantom center) were used as in Khellaf et al. [5]. The beam size was set to fully cover the phantom. For each pCT simulation, 180 projections were acquired equidistantly over a range of 360°. Similar to Kaser et al. [9], the focus was to evaluate the method using a parallel beam geometry. Since other studies also use a cone-beam geometry [5,10], this setting was also investigated in one test scenario for an ideal data set and the high resolution module. In this case, the source-isocenter-distance was set to 2m (50cm in case of the parallel geometry).

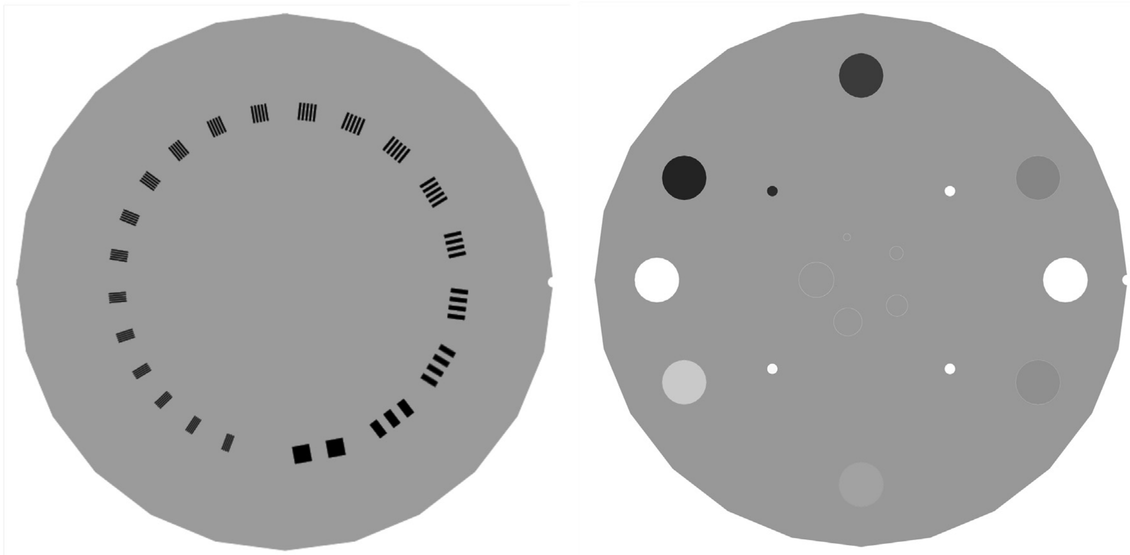

Figure 3. Left: high resolution module (CTP528). Right: sensitometry module (CTP404).

Additionally, a CT scan of the 'phantom patient for stereotactic end-to-end verification (STEEV)' (CIRS, Norfolk, VA, USA) [20], further referred to as CIRS phantom, was imported into a parallel-beam Monte Carlo simulation using GATE [21]. The phantom materials were converted to tissues in the simulation using the conversion table integrated in the simulation platform, which follows the correlation of HU and tissues suggested by Schneider et al. [22]. The analyzed phantom slice is displayed in Fig. 4. 90 radiographs (0 ° to 180° in steps of 2°) using 50 protons/mm^2 (non-ideal setup) were used as input data for the ASD-POCS reconstruction algorithm (with maximum iterations set to 15). By doing so, the performance of the pre-reconstruction binning code and subsequent reconstruction for biological materials and low input data could be evaluated. In contrast to the setup displayed in Fig. 2, the innermost tracking detectors were set 50 cm apart for the CIRS phantom.

As in Collins-Fekete et al. [10], all simulated data were filtered with the 3σ cuts based on exit proton direction and energy, as proposed by Schulte et al. [23].

Figure 4. Slice of the CIRS patient phantom (as obtained from an X-ray CT scan).

2.2 Proton radiography and CT reconstruction methods

In Collins-Fekete et al. [10], a high resolution proton radiograph is calculated using a maximum likelihood method by assigning the WEPL of each proton to all channels k (cf. Fig. 1) it passed according to its path estimate. The water-equivalent thickness (WET) per channel is therefore obtained as

$$\mathrm{WET}_k = \frac{\sum_n^N \frac{l_{k,n}^2}{L_n^2}\mathrm{WEPL}_n}{\sum_n^N \frac{l_{k,n}^2}{L_n^2}}, \tag{1}$$

with each proton n (of total N protons passing a channel) contributing to a channel k with a weighting factor depending on the length l it has spent in a certain channel while passing a total length L_n. L_n was set to be equal to the distance between the two innermost detector planes in all cases. From that, a high resolution proton radiograph is obtained that can be further used as input for any X-ray CT reconstruction algorithm.

Based on the findings in Kaser et al. [9], where ASD-POCS [24] resulted in superior reconstruction results than other algorithms for limited proton projection data, this algorithm was used for the reconstructions in this work. For the sensitometry module, a voxel size of $0.5 \times 0.5 \times 0.5$ mm was chosen, whereas the high resolution module was reconstructed with a finer voxel size of $0.25 \times 0.25 \times 0.25$ mm^3 due to the smaller inserts. Following the size of the original CT scan, the CIRS patient phantom was reconstructed with a voxel size of $0.68 \times 2.0 \times 0.68$ mm^3.

2.3 TIGRE toolbox and code implementation

TIGRE [8] is an open-source toolbox providing multiple direct and iterative reconstruction algorithms for X-ray CT (parallel and cone-beam geometry). The code is arranged in a modular structure: The bottom layer, which includes forward and back-projection operators of the reconstruction algorithms, is written in the Compute Unified Device Architecture (CUDA) language (using C++) and hence runs on GPUs. The top layers, which are intended to be more user-friendly and easy to modify or adjust, are implemented in Matlab and python and incorporate algorithms and user scripts, with a C++ communication layer between them.

To obtain high resolution proton radiographs as described by Collins-Fekete et al. [10], no hull was applied, since, in radiographic images, the convex hull [12,13] of the object cannot be expected to be known. The path estimate (an optimized cubic spline as in Fekete et al. [11]) was therefore calculated between the two innermost tracking detectors, making the approach strongly dependent on the detector distances. However, since the focus of this work is the reconstruction of a 3-dimensional image, as in other proton and ion CT reconstruction approaches [4,18], the convex hull can be expected to be known. Therefore, two approaches were implemented in the pCT extension for the TIGRE toolbox:

- **Original (orig.):** This approach follows the original method for high resolution parallel and cone-beam proton radiography, as described by Collins-Fekete et al. [10]. This approach can be used if a radiograph has to be generated and the convex hull of the object is unknown. For the parallel beam, all channels share the same length (parallel lines), whereas the channel size for the cone-beam geometry increases with the opening angles.
- **Improved (imp.):** A cylindrical hull surrounding the object is applied for the calculation of the proton radiograph. This hull implementation does not correspond to the convex hull for complex shapes like a human head, and will therefore have to be refined in the future. The optimized cubic spline is only calculated inside the hull, whereas a straight-line approach is used in air.

With the improved approach, the assignment of a proton WEPL to channels, which only contributed little to the particle's energy loss, can be rectified by introducing an additional weighting factor to the contribution of protons to the respective channel (see Fig. 5). If the proton passed through the channel in air, the contribution factor $l_{k,n}^2/L_n^2$ is assigned with an additional weight $w_{\text{air}} = 0.00479$ which corresponds to the RSP of air according to Berger et al. [25]. Inside the hull, the weighting factor is set to $w_{\text{hull}} = 1$, corresponding to the RSP of water, which is a typical reference material for human tissues. If a channel lies fully outside (or inside) the hull, the factor will cancel out naturally.

The code extension was tested on an Nvidia RTX 4000. It was implemented following the layer structure of the TIGRE toolbox itself, thus, the calculation of the proton path estimate and the channel intercepts are implemented using CUDA and hence run accelerated on a GPU. For the user, a Matlab script is provided that invokes this function.

The object-surrounding hull was realized as a rotational ellipse given by

$$\frac{(x\cos(\alpha) - z\sin(\alpha))^2}{a^2} + \frac{(x\sin(\alpha) + z\cos(\alpha))^2}{b^2} = 1, \tag{2}$$

where a, b, the rotation angle α as well as a maximum height h (see Fig. 6) of the hull can be freely chosen. For future code refinement, this simplified hull surrounding the object will have to be replaced by custom convex hulls [12,13] to match with different phantom shapes, ideally. If requested, the resulting radiographs can be directly used to reconstruct a 3D image using the algorithms already implemented in TIGRE.

One crucial point when calculating the radiographs is the maximum number of allowed channel intercepts per proton. In contrast to C++, where one entry after another can be simply added to a dynamic vector, CUDA does not allow for

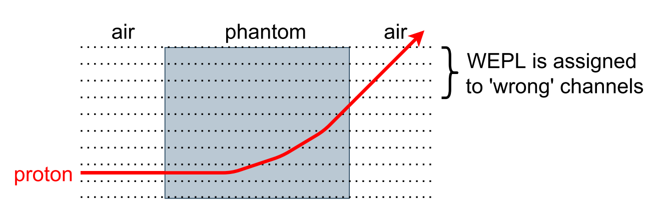

Figure 5. Using the original methodology for high resolution proton radiography as described by Collins-Fekete et al. [10], a proton WEPL could be wrongly assigned to multiple channels outside the hull that did not mainly contribute to the proton's energy loss. In the sketch, the channels for a parallel beam geometry are displayed.

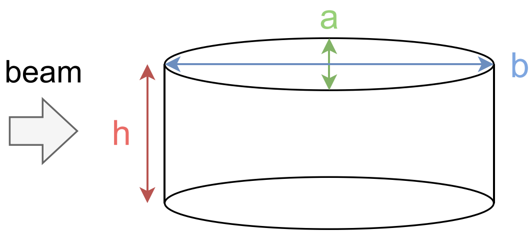

Figure 6. Definition of the implemented hull option. The hull can be rotated alongside with the projection angle.

dynamic memory allocation on the local memory, where the channel intercepts per proton are calculated. Setting the number of allowed intercepts to an unnecessarily high value increases the run time and blocks an unnecessarily high amount of memory. Therefore, the array size for channel intercepts provides a powerful tool to influence run time and appearance of the final result.

To define a default size for the intercepts arrays, Geant4 simulations of water blocks from 50 mm to 350 mm irradiated at 151 MeV to 281 MeV, respectively, were performed using detector thicknesses of 100 μm to 500 μm (to cover a realistic range for silicon detectors) and assuming a channel cross-sectional area of $0.25 \times 0.25\ \text{mm}^2$. Between the cuboid water phantom and the innermost detectors, a distance of 10 cm was set. 10^6 protons were recorded per projection and the number of intercepts per proton was recorded upstream of the phantom (air), in the phantom (water) and downstream of the phantom (air). The maximum number of intercepts covering at least 99% of proton path estimates was then used as default size for the channel intercepts vectors. Note that these default sizes may not be suitable for all pCT setups. In case of large phantoms or large distances between the trackers, larger intercepts vector sizes may be necessary. Therefore, during the compile time, the user still has the option to adapt the intercepts vector sizes. However, as reported for the phantoms investigated in this work, the obtained default intercepts vector sizes are large enough (see Section 3.1).

2.4 Image analysis

As in Kaser et al. [9] and Volz et al. [18], the value of the modulation transfer function (MTF) at the line pair inserts for the high resolution module was approximated using

$$\mathrm{MTF}(i) \approx \frac{\langle \mathrm{RSP}_{\max}(i) - \mathrm{RSP}_{\min}(i) \rangle}{\mathrm{RSP}_{\mathrm{ref,max}} - \mathrm{RSP}_{\mathrm{ref,min}}}, \tag{3}$$

where $\mathrm{RSP}_{\max}(i)$ and $\mathrm{RSP}_{\min}(i)$ are the maximum and minimum RSP values measured for a specific line pair insert i using the central slice of the reconstructed phantom. As this definition corresponds to an approximation of the MTF, resulting values are labelled with the $\approx$ sign. The reference values $\mathrm{RSP}_{\mathrm{ref,max}}$ and $\mathrm{RSP}_{\mathrm{ref,min}}$ for aluminum and acrylic were obtained via Geant4 simulations by placing absorber blocks of the investigated material in front of a water absorber and by performing a simulated RSP measurement using the R80 method [16]. In addition, reference values without an absorber block were measured. The observed range shift (between the measurements with and without the absorber block) and the knowledge of the absorber thickness can be used to evaluate the RSP of a material. For aluminum and acrylic, they were found to be 1.165 and 2.125, respectively. For the high resolution module, MTF values up to $i = 8$, i.e. 8 lp/cm, were analyzed. As in Collins-Fekete et al. [10], the $\mathrm{MTF}_{10\%}$ was taken as the lower threshold to define the line pair resolution. If the contrast of a line pair insert in the reconstructed image decreased below 10% according to Eq. (3), it was regarded as non-resolvable.

Similar to Collins-Fekete et al. [26] and Dickmann et al. [27], the radial dependence of the noise within the central slice of the phantom cylinder was analyzed. Following their approaches, the sample standard deviation σ_{meas} of the RSP was analyzed in equidistant regions of interest ($8 \times 1 \times 8$ voxels) from the phantom center to the edge.

For the sensitometry module, the RSP accuracy was evaluated by calculating RSP mean and standard deviation in the outer inserts made from Acrylic, LDPE (Low Density Polyethylen), PMP (Polymethylpentene), Polystyrene, Delrin® (Polyoxymethylene) and Teflon® (Polytetrafluoroethylene). As in Ulrich-Pur et al. [19], the analysis volume consisted of a base area of $6 \times 6\ \text{mm}^2$ and the innermost 15 slices of the reconstructed image and was located in the center of the respective insert. Again, reference RSP values were obtained from a simulated R80 measurement [16]. As in Ulrich-Pur et al. [19], they were determined to be 1.165, 0.987, 0.890, 1.043, 1.371 and 1.85, respectively. As a quality measure, the relative error of the mean RSP,

$$\epsilon_{\mathrm{rel},j} = \frac{\mathrm{RSP}_{\mathrm{meas},j} - \mathrm{RSP}_{\mathrm{ref},j}}{\mathrm{RSP}_{\mathrm{ref},j}}, \tag{4}$$

where the measured average $\mathrm{RSP}_{\mathrm{meas},j}$ per insert j was compared to its reference value $\mathrm{RSP}_{\mathrm{ref},j}$, was calculated. From all relative errors, the mean absolute percentage error (MAPE) for the six inserts was calculated as

$$\mathrm{MAPE} = \frac{1}{6}\sum_{j=1}^{6} |\epsilon_{\mathrm{rel},j}|. \tag{5}$$

Furthermore, the signal-to-noise ratio (SNR) in each insert was calculated via

$$\mathrm{SNR}_j = \frac{\mathrm{RSP}_{\mathrm{meas},j}}{\sigma_{\mathrm{meas},j}}, \tag{6}$$

using the standard deviation $\sigma_{\mathrm{meas},j}$ of the measured RSP values within each measurement.

For the CIRS patient phantom, an RSP reference map was generated by performing an R80 measurement [16] for all the phantom's materials in a respective Monte Carlo simulation, serving as ground truth data. By subtracting the reconstructed images from the reference map RSP_{ref}, the absolute RSP error (ΔRSP) was obtained for each voxel i as

$$\Delta RSP_i = RSP_{meas,i} - RSP_{ref,i}. \tag{7}$$

By calculating the sum of the absolute values of ΔRSP_i of all voxels in a region of interest (ROI) and dividing by the respective voxel count, an absolute average value for the absolute RSP error for this ROI can be obtained.

3 Results

3.1 Channel intercepts

As stated in Section 2.2, the number of channel intercepts per proton was studied with a Geant4 simulation. In the simulations, the necessary vector size for all intercepts was recorded for various beam energies and water phantom thicknesses. From these findings, default values of 10 channel intercepts for the straight-line path upstream of the phantom, 220 intercepts for the cubic spline path and 100 intercepts for the straight-line path downstream of the phantom were set. This default numbers were scaled by the respective pixel size set by the user with respect to a default size of 0.25×0.25 mm^2. During compile time, the user is asked to change these values per command line input if needed. If for a proton path estimate, more than the given channel intercepts are obtained in the calculation process of a proton radiograph, the proton is not used for the respective radiograph. For the reconstructions in this work, this applied to 1.5% of the proton tracks at most for one radiograph.

3.2 Catphan® reconstructions

As outlined in Section 2.1, the focus of the analysis was on a parallel beam geometry. However, at the end of Section 3.2.2, the results of a reconstruction using a cone-beam geometry are presented.

3.2.1 Sensitometry module

As described in Section 2.1, ideal and non-ideal projection data were generated with Geant4 and used for the calculation of high resolution proton radiographs as well as for the subsequent pCT reconstruction. The resulting central slices are displayed in Fig. 7 (ideal setup) and Fig. 8 (non-ideal setup). In both cases, the result using the original (no hull) and improved (with an object-surrounding cylindrical hull) approach to calculate the proton radiographs based on the maximum likelihood approach are displayed. While a visual difference can hardly be observed in the images, the detailed analysis of RSP accuracy (Table 1) and and SNR (Table 2) does show differences between the reconstructions.

Although the MAPE was found to be below 1% for all reconstructions, the relative errors per insert depended on the reconstruction. For the original method, errors up to 1.28% (Teflon®, ideal projection data) and 1.13% (Teflon®, non-ideal projection data) were found. The maximum relative error for the improved approach using an object-surrounding cylindrical hull and channel weighting was found to be 0.36% (Teflon®, ideal projection data) and 0.47% (Delrin®, non-ideal projection data) which is below the errors received from the original method. This finding is corroborated by the MAPE, which is always smaller for reconstructions using the improved approach instead of the original approach.

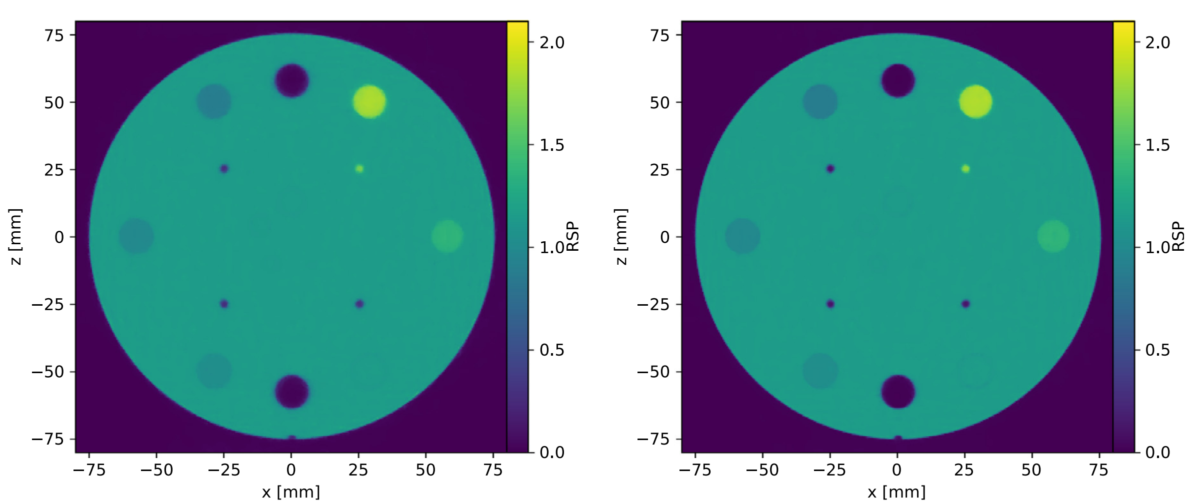

Figure 7. Reconstructed central slices of the sensitometry module (ideal conditions). Left: without hull. Right: with an object-surrounding cylindrical hull.

Please cite this article as: , Extension of the open-source TIGRE toolbox for proton imaging, Z Med Phys, https://doi.org/10.1016/j.zemedi.2022.08.005

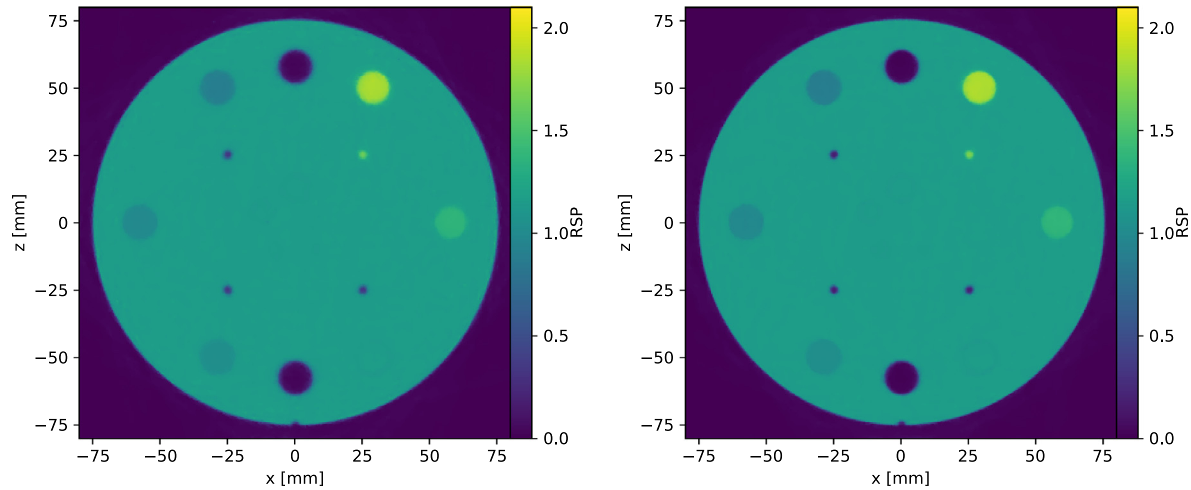

Figure 8. Reconstructed central slices of the sensitometry module (non-ideal conditions). Left: without hull. Right: with an object-surrounding cylindrical hull.

Table 1
RSP errors within the sensitometry inserts. 15 slices and an area of 6 mm × 6 mm were used per insert for the analysis. The analysis of the ideal data set has been marked with the subscript *i*, whereas the analysis of the non-ideal data set was marked with the subscript *n*. *Original* (orig.) refers to the original method for proton radiography described by Collins-Fekete et al. [10] (without hull). *Improved* (imp.) refers to the reconstruction results with an object-surrounding cylindrical hull and channel weighting.

Method	Acrylic	PMP	LDPE	Teflon®	Delrin®	Polyst.	MAPE
orig.$_i$	−0.12%	0.12%	0.16%	−1.28%	−0.49%	0.16%	0.39%
imp.$_i$	−0.04%	−0.34%	0.01%	−0.36%	−0.10%	0.01%	0.14%
orig.$_n$	0.02%	0.80%	0.35%	−1.13%	−0.41%	0.05%	0.46%
imp.$_n$	0.12%	0.44%	−0.26%	−0.33%	0.47%	−0.10%	0.29%

Table 2
SNR within the sensitometry inserts. 15 slices and an area of 6 mm × 6 mm were used per insert for the analysis. The analysis of the ideal data set has been marked with the subscript *i*, whereas the analysis of the non-ideal data set was marked with the subscript *n*. *Original* (orig.) refers to the original method for proton radiography described by Collins-Fekete et al. [10] (without hull). *Improved* (imp.) refers to the reconstruction results with an object-surrounding cylindrical hull and channel weighting.

Method	Acrylic	PMP	LDPE	Teflon®	Delrin®	Polystyrene	Average SNR
orig.$_i$	301.7	219.5	192.6	170.3	245.3	250.7	230.0
imp.$_i$	283.0	309.6	198.5	257.3	221.1	312.5	263.7
orig.$_n$	308.8	236.0	210.5	167.2	300.4	327.2	258.4
imp.$_n$	217.4	215.3	227.5	324.4	256.7	246.1	247.9

With reference to the SNR, the reconstruction results of this work are generally expected to benefit from the ASD-POCS algorithm that is designed to result in low-noise images [8]. Apart from the chosen reconstruction algorithm, the imaging dose has a strong influence on the SNR. As no further dose considerations were taken into account in this work, SNR values for all reconstructions were only compared relatively. It could be observed that the average value of the SNR for the reconstruction using the radiographs obtained with the improved approach as input is on average higher for the ideal setup. On the other hand, for the non-ideal setup, the original approach yields a higher average value (see Table 2). Hence, no general improvement in the average SNR value could be observed using the improved approach. However, the spread of the SNR values for different inserts was clearly higher in the case of the original approach whereas for the improved approach, the SNR values of the single values were more balanced, as again seen in Table 2.

The binning time for each radiograph was recorded to be less than or equal to 0.25 s for the sensitometry module. For all 180 radiographs, this sums up to a total calculation time of 45 s. However, this does not include the time for loading the projection data into Matlab, which depends on the hardware storage and file format used. The subsequent reconstruction time for the sensitometry module (with a volume of $320 \times 100 \times 320$ voxels) from these radiographs was between 1 min and 2 min on one GPU (number of iterations until convergence depended on the data set and was found to be between 10 and 14). This reconstruction time results solely from the algorithm implementation of ASD-POCS in TIGRE and could be further reduced. A problem-specific implementation in TIGRE could further reduce the reconstruction time as shown, e.g., in Hatamikia et al. [28].

3.2.2 High resolution module

The central slices of the reconstructed high resolution module are displayed in Figs. 9 and 10 for ideal and non-ideal projection data, respectively. To visually highlight the differences between the results obtained with the two different maximum-likelihood approaches as input, the 5 lp/cm insert was highlighted and zoomed in. The images show that the improved approach with an object-surrounding cylindrical hull (right in the plots) generates improved reconstruction results compared to the method without this hull.

To quantify this observation, the MTF of the first eight line pair inserts was approximated according to Eq. (3). The results are plotted in Fig. 12. For the original method without an object-surrounding cylindrical hull, the MTF decreased to ≈11.5% for the 5 lp/cm insert when non-ideal data were used. The approach including a hull still yielded an MTF value of ≈15.8% for this insert. Using the latter method and ideal projection data, an MTF value of ≈25.8% was observed for the 5 lp/cm insert. For the reconstruction of ideal projection data using the original approach, the MTF was found to be ≈13.1% for the 5 lp/cm insert, which is well below the result of the reconstruction using radiograph data with an object-surrounding cylindrical hull.

The binning time per reconstructed radiograph was at most 0.5 s for the high resolution module, whereas the reconstruction time for the module (with a volume of $640 \times 200 \times 640$ voxels) from these radiographs was approximately 6 min to 10 min on one GPU, depending on the data set.

As stated in Section 2.1, one idealized data set using a cone-beam geometry was generated and tested. The resulting central slices using the original and improved approach to generate radiographs as pCT reconstruction input data are displayed in Fig. 11. Approximate MTF values for the first eight line pair inserts are displayed in Fig. 12. For the cone-beam geometry, the advantages of the improved method (with an object-surrounding cylindrical hull) are again apparent: for the original approach, the MTF value of the 3lp/cm insert decreased to ≈46.8%, whereas the improved approach still yielded a value of ≈56.3%. Using the latter approach, an MTF value of ≈13.8% could still be achieved at the 8lp/cm insert, whereas for the original approach, the 7lp/cm insert was the highest one with an MTF value above the $MTF_{10\%}$ (≈11.9%).

For all reconstructions of the high resolution module, the radial dependence of the noise was analyzed from the phantom center to the edge by investigating the standard devia-

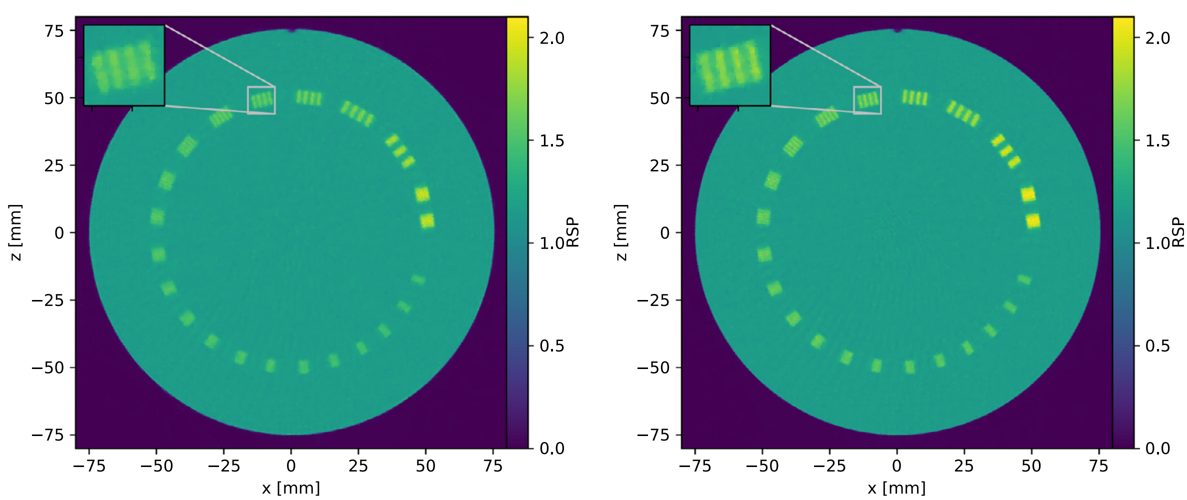

Figure 9. Reconstructed central slices of the high resolution module (ideal conditions). Left: without hull. Right: with an object-surrounding cylindrical hull.

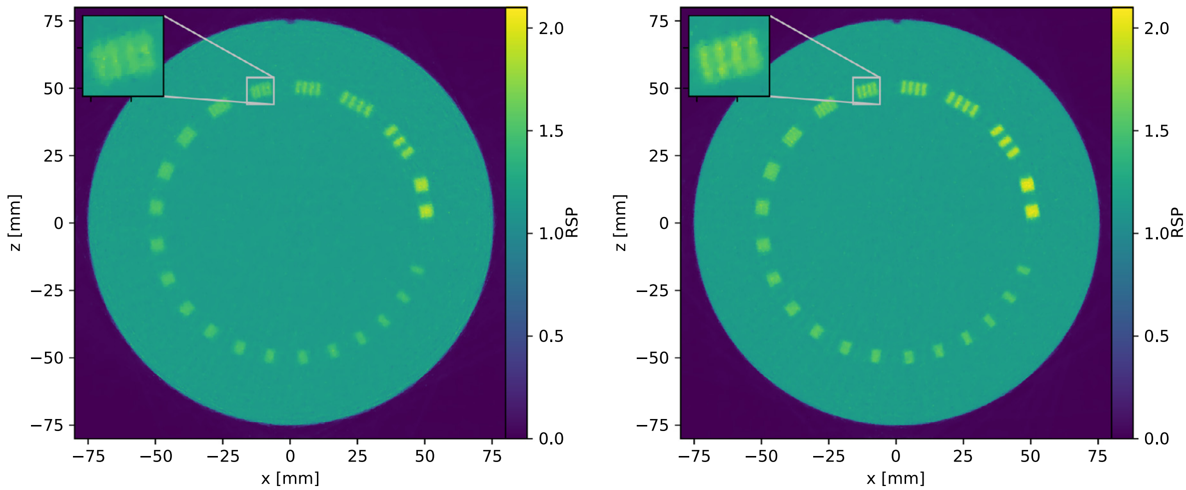

Figure 10. Reconstructed central slices of the high resolution module (non-ideal conditions). Left: without hull. Right: with an object-surrounding cylindrical hull.

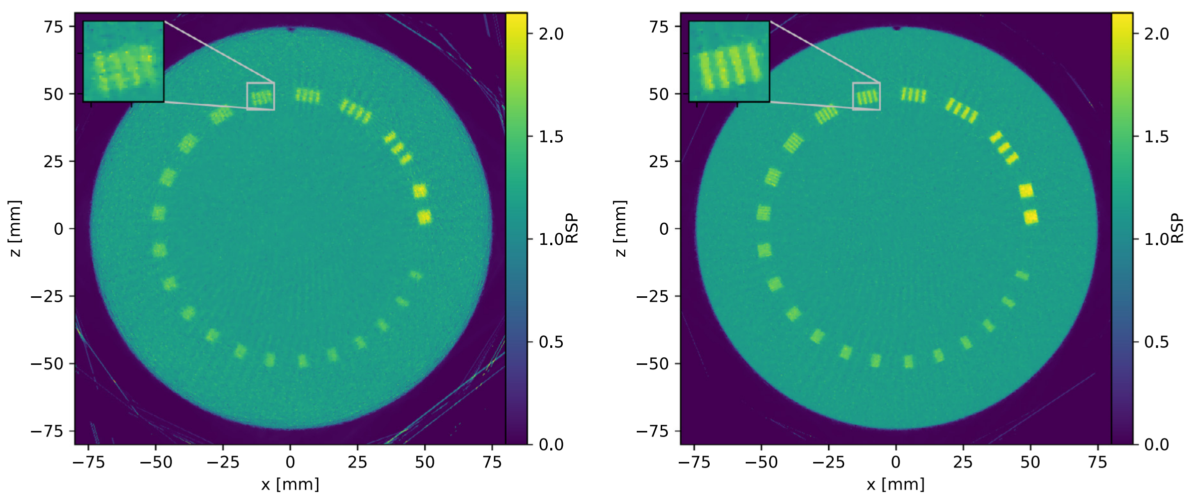

Figure 11. Reconstructed central slices of the high resolution module (ideal conditions) using a cone-beam geometry. Left: without hull. Right: with an object-surrounding cylindrical hull.

tion σ_{meas} of the reconstructed values in equidistant ROIs ($8 \times 1 \times 8$ voxels) relative to the average within this ROI (see Fig. 13). For the reconstructions using a parallel beam, no trend of the noise towards the edges could be observed. Regarding the reconstructions using a cone beam, a higher noise level was generally recorded with respect to the reconstructions obtained with a parallel beam. For the reconstruction using the original approach (no object-surrounding cylindrical hull), an increase of the noise was observed towards the edge.

3.2.3 CIRS patient phantom

The RSP accuracy was analyzed for one slice in the reconstructed CIRS patient phantom. The absolute RSP error was obtained by subtracting the reconstructed slices as displayed in Fig. 14 from a reference RSP map. The result of this subtraction (see Eq. (7)) is displayed in Fig. 15, where two ROIs containing material transitions with potentially higher RSP errors were chosen to illustrate the partial volume effect [29].

Visually, these transitions result in lower ΔRSP values when an object-surrounding cylindrical hull is used in the binning process, although the implemented hull does not ideally match with the head shape of the phantom. On average, in ROI_A, the absolute value of ΔRSP using the original approach was found to be 0.099, whereas a value of 0.067 was recorded for the improved approach. For ROI_B, the absolute average ΔRSP was found to be 0.146 and 0.120, respectively.

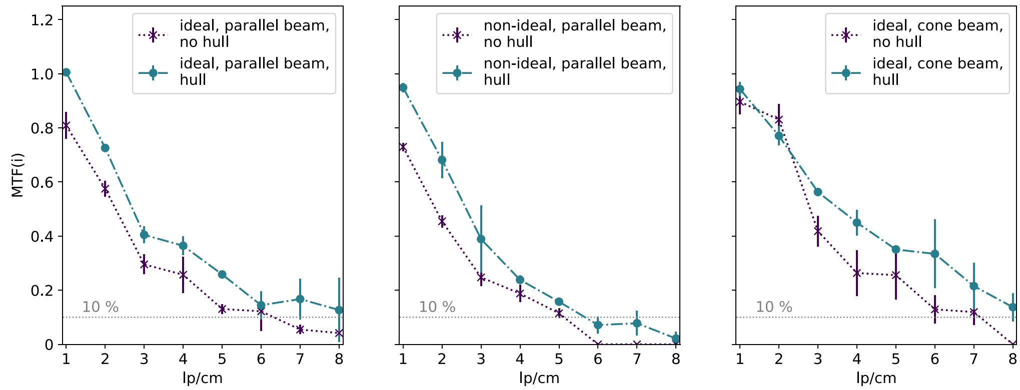

Figure 12. Approximate MTF values of line pairs (i) of the high resolution module for all investigated modalities (ideal and non-ideal conditions with and without using an object-surrounding cylindrical hull to generate proton radiographs). The lower limit ($MTF_{10\%}$) is displayed as a dotted gray line in the plot. The left and the middle plot represent results with a parallel proton beam, and the plot on the right displays the results obtained with a cone-beam. The uncertainty of the MTF values corresponds to one standard deviation.

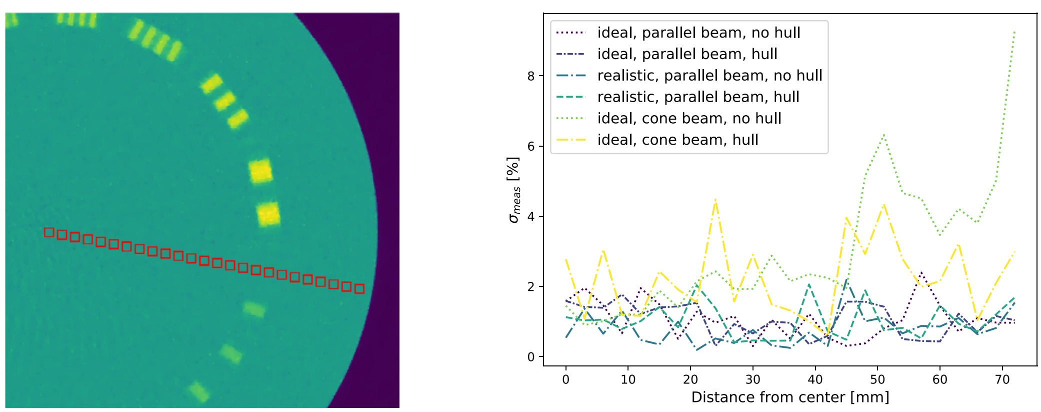

Figure 13. Radial dependence of the noise for the high resolution module. σ_{meas} for a ROI is given relative to the average in this ROI.

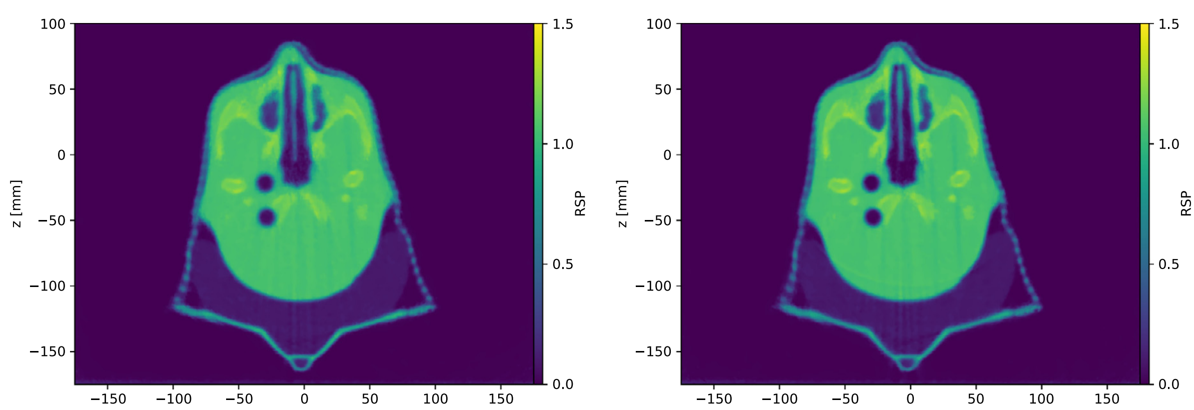

Figure 14. Reconstructed CIRS patient phantom. Left: without hull, right: with an object-surrounding cylindrical hull.

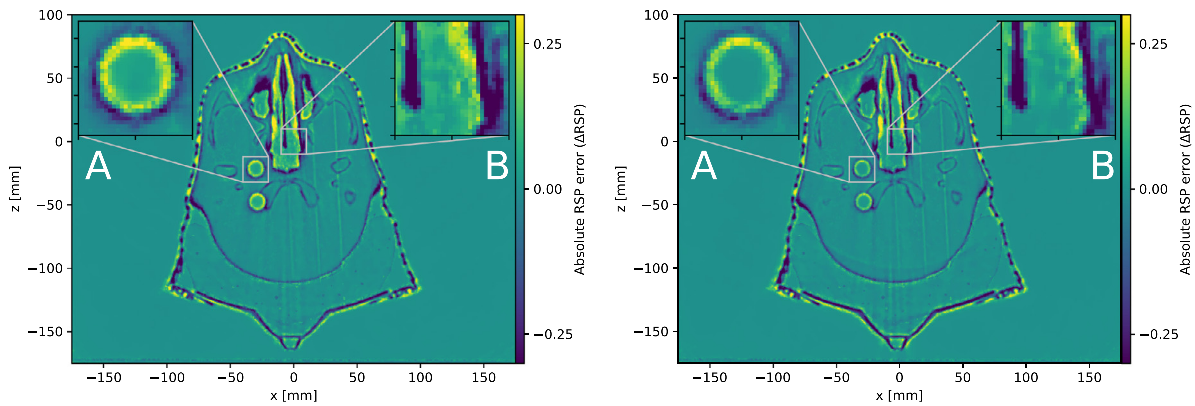

Figure 15. Absolute RSP error as obtained by subtraction from a reference RSP map. Left: without hull, right: with an object-surrounding cylindrical hull.

The binning time for each reconstructed radiograph of the CIRS phantom amounted to 0.7 s at most, followed by a reconstruction time of approximately 100 s on one GPU (with a reconstruction volume of 512 $\times$ 145 $\times$ 512 voxels) from these radiographs.

4 Discussion

To implement efficient pCT image reconstruction in TIGRE, a code extension was added to the toolbox. The extension allows calculating high resolution ion radiographs based on the method described by Collins-Fekete et al. [10] who used an optimized cubic spline as the proton path estimate and a maximum likelihood estimator to calculate the WET of each pixel in a proton radiograph. A further improvement of the reconstruction results of this work could be achieved by adding an object-surrounding cylindrical hull and implementing a channel weighting as optional parameters for the reconstruction of a radiograph. The code was made available as part of the TIGRE toolbox in GitHub[1], offering the possibility for other research groups to use a fast and accurate open-source pCT reconstruction. As input parameters, the proton position, direction, WEPL, and geometry parameters such as detector distances and requested pixel size are required.

Both approaches were tested by reconstructing proton radiographs using ideal and non-ideal projection data of two Catphan® modules (high resolution and sensitometry) that were obtained from Geant4 Monte Carlo simulations. The radiographs (180 per reconstruction) were further used as input for the ASD-POCS algorithm instead of using a direct reconstruction as in Collins-Fekete et al. [10]. As shown in Sections 3.2.1 and 3.2.2, the proposed method using an object-surrounding cylindrical hull to calculate the radiographs was able to improve reconstruction results in terms of RSP accuracy and line pair contrast. The MAPEs of the RSP inserts of the sensitometry module were found to be between 0.14% and 0.46% which is slightly below the value found in Dedes et al. [30] (0.55% for measurement data and 0.69% for a corresponding Monte Carlo simulation), where distance-driven binning [4] was used for the reconstruction. In Götz et al. [31], a MAPE of 0.19% was reported for a reconstruction (using again distance-driven binning) of an ideal data set of the sensitometry module and 0.59% for a realistic data set (using a particle fluence of 104 protons per mm^2 per projection and a total of 360 projections).

Up to 8lp/cm could be resolved with the improved approach outlined in this work (using a cone beam or parallel geometry and an idealized data set). This is above the 5.55lp/cm that were reported in Collins-Fekete et al. [10]. However, it has to be stated that the results are not directly comparable, as the high resolution phantom was simulated with a 20 cm diameter in Collins-Fekete et al. [10] and the authors stated that no detector effects were simulated. In the present work, the number of resolvable line pair inserts strongly depended on the data set used: for the non-ideal data set, the $MTF_{10\%}$ was found slightly below 6lp/cm, which corresponds well to the value in Collins-Fekete et al. [10]. Maximum RSP values for the line pair inserts were found to be higher than the ones observed for a reconstruction using the original approach to create input data [5] (idealized data set, 720 projections, 225 protons per mm^2 per projection). For the 1lp/cm insert, maximum values of approximately 1.7 were reported, whereas they were found to be in the range of 2.0 to 2.1 using the improved approach (with an object-surrounding cylindrical hull and channel weighting) presented in this work (valid for cone-beam

[1] https://github.com/CERN/TIGRE.

and parallel beam). For the 3lp/cm insert, in Khellaf et al. [5] a maximum RSP value of approximately 1.6 was displayed for the reconstruction using the original approach to generate input data, whereas in this work, maximum RSP values between 1.75 and 1.82 (parallel beam) or 1.88 and 1.91 (cone-beam) were observed when an object-surrounding cylindrical hull and channel weighting were considered for the processing of the input data for the reconstruction. The resulting maximum RSP values lie closer to the reference value of 2.125 with the approach presented in this work, although fewer projections (180 instead of 720) were used.

The radial dependence of the image noise in the high resolution module was analyzed by investigating the standard deviation σ_{meas} relative to the average RSP in equidistant ROIs ($8 \times 1 \times 8$ voxels) from the phantom center to the edge. For the reconstructions using a parallel beam, the image noise did not show an increase towards the phantom edge, which corresponds well to the radial dependence of noise as observed by Rädler et al. [32]. On the other hand, Dickmann et al. [27] found increased noise towards the phantom edges in their study. However, in contrast to Rädler et al. [32] and the present work, they accounted for noise in the energy detection process (energy straggling in the calorimeter slices) and also used a realistic model for the incident beam obtained from experimental tracking data. Both mentioned studies used distance-driven binning and a filtered backprojection [4] for reconstruction, whereas the ASD-POCS used in this work is expected to suppress image noise [8]. In the study presented in this work, a higher noise level was recorded for reconstructions using a cone-beam geometry with respect to the reconstructions obtained with a parallel beam. For the reconstruction using the original approach (no object-surrounding hull), an increase of the noise was observed towards the edge (visible as streak artifacts, as seen in Fig. 11 (left).

To investigate the code performance for biological materials, a CT scan of the CIRS patient phantom was incorporated as a phantom in a Monte Carlo simulation. The number of projections was reduced to 90, and the number of primary particles to 50 mm^{-2} to model a CT scan with low statistics input data. Although the improved reconstruction volume does not ideally fit the object hull of the given head shape, the reconstruction could be improved, as seen in the analysis of RSP errors in two ROIs (Fig. 15). Methods to better approximate the object hull for pCT reconstruction have been described in Schultze et al. [12,13] and should be used for the future improvement of the approach implemented in TIGRE.

Using an Nvidia RTX 4000, the newly added code extension to the TIGRE toolbox was able to calculate one proton radiograph from approximately 10^6 protons in less than 0.5 s, hence 5 s for 10^7 protons. In Fekete et al. [10], a calculation time of over 4 min was reported for one radiograph obtained from 10^7 protons. Although the calculation time is strongly dependent on the phantom size (thicker phantoms lead to longer calculation times), it is obvious that the CUDA implementation allows for a significant increase in speed. Furthermore, by setting the maximum number of allowed intercepts, the user can control calculation time to some extent by cutting a few percent (strongly scattered protons) of the initial data set. Small differences in the calculation times were observed depending on the approach used to reconstruct the proton radiographs (with or without an object-surrounding cylindrical hull). For the high resolution module, for example, the binning time was observed to be in the range of 0.3 s to 0.4 s for the original approach, whereas for the improved approach, a calculation time between 0.4 s and 0.5 s was obtained. Furthermore, a slightly higher data rejection rate due to the intercept vector size was observed when an object-surrounding cylindrical hull was used. For example, 0.8% of the initial ideal data set of the high resolution module were cut for the improved approach, compared to 0.1% without hull.

As the radiographs calculated in this work already contain the proton path estimate, the projections can be directly used as input for the reconstruction algorithms already implemented in TIGRE. This allows for fast overall reconstruction time, since the reconstruction algorithm does not have to deal with list-mode, but already binned proton data. Reconstruction time for the final image reconstruction (after already having created the proton radiographs as input data) was below 2 min (parallel beam geometry, $320 \times 100 \times 320$ voxels) using one GPU. However, the proposed toolbox allows for further acceleration using multiple GPUs.

Next steps to improve the code extension for the TIGRE toolbox include the implementation of multi-GPU use and the implementation of a sophisticated model for the actual convex hull of the object-to-be-imaged [12,13] that is able to accurately represent complex shapes like a human head. While ASD-POCS has shown promising results in the initial [9] and the current study, alternative edge preserving total variations methods, such as the adaptive weighted (Aw) total variation (TV) using ASD-POCS [33] as well as AwPCSD [34] should be evaluated to investigate the superiority of their performance in edge preservation and noise cancellation properties.

5 Conclusion

To efficiently use TIGRE for proton CT image reconstruction, a GPU-accelerated code extension calculating proton radiographs based on a maximum likelihood approach was implemented in the reconstruction toolbox. Using these radiographs as input data for the already integrated CT

Please cite this article as: , Extension of the open-source TIGRE toolbox for proton imaging, Z Med Phys, https://doi.org/10.1016/j.zemedi.2022.08.005

algorithms in TIGRE allows for proton CT image reconstruction with high spatial resolution and RSP accuracy. The newly implemented code was successfully tested with data obtained from Monte Carlo simulations.

Declaration of Competing Interest

The authors declare that they have no known competing financial interests or personal relationships that could have appeared to influence the work reported in this paper.

Acknowledgements

This project received funding from the Austrian Research Promotion Agency (FFG), Grant No. 875854.

The authors would like to thank Barbara Knäusl (MedUni Wien) and Markus Stock (MedAustron) for providing the CT scan of the CIRS patient phantom. Furthermore, the authors would like to thank Paul Sommerer for his contribution in generating the RSP reference map of this phantom.

References

[1] Schneider U, Pedroni E, Lomax A. The calibration of CT Hounsfield units for radiotherapy treatment planning. Phys Med Biol 1996;41(1):111–124. https://doi.org/10.1088/0031-9155/41/1/009.

[2] Schulte R, Bashkirov V, Li T, Liang Z, Mueller K, Heimann J, et al. Conceptual design of a proton computed tomography system for applications in proton radiation therapy. IEEE Trans Nucl Sci 2004;51(3):866–872. https://doi.org/10.1109/TNS.2004.829392.

[3] Schneider U, Besserer J, Pemler P, Dellert M, Moosburger M, Pedroni E, et al. First proton radiography of an animal patient. Med Phys 2004;31(5):1046–1051. https://doi.org/10.1118/1.1690713.

[4] Rit S, Dedes G, Freud N, Sarrut D, Létang JM. Filtered backprojection proton CT reconstruction along most likely paths. Med Phys 2013;40(3):031103. https://doi.org/10.1118/1.4789589.

[5] Khellaf F, Krah N, Létang JM, Collins-Fekete CA, Rit S. A comparison of direct reconstruction algorithms in proton computed tomography. Phys Med Biol 2020;65(10):105010. https://doi.org/10.1088/1361-6560/ab7d53.

[6] Hansen DC, Sørensen TS, Rit S. Fast reconstruction of low dose proton CT by sinogram interpolation. Phys Med Biol 2016;61(15):5868. https://doi.org/10.1088/0031-9155/61/15/5868.

[7] Karbasi P, Cai R, Schultze B, Nguyen H, Reed J, Hall P, et al. A highly accelerated parallel multi-gpu based reconstruction algorithm for generating accurate relative stopping powers. In: 2017 IEEE Nuclear Science Symposium and Medical Imaging Conference (NSS/MIC). IEEE; 2017. p. 1–4. https://doi.org/10.1109/NSSMIC.2017.8532871.

[8] Biguri A, Dosanjh M, Hancock S, Soleimani M. TIGRE: a MATLAB-GPU toolbox for CBCT image reconstruction. Biomed Phys Eng Exp 2016;2(5):055010. https://doi.org/10.1088/2057-1976/2/5/055010.

[9] Kaser S, Bergauer T, Birkfellner W, Burker A, Georg D, Hatamikia S, et al. First application of the GPU-based software framework TIGRE for proton CT image reconstruction. Phys Med 2021;84:56–64. https://doi.org/10.1016/j.ejmp.2021.03.006.

[10] Collins-Fekete CA, Brousmiche S, Portillo SK, Beaulieu L, Seco J. A maximum likelihood method for high resolution proton radiography/proton CT. Phys Med Biol 2016;61(23):8232. https://doi.org/10.1088/0031-9155/61/23/8232.

[11] Fekete CAC, Doolan P, Dias MF, Beaulieu L, Seco J. Developing a phenomenological model of the proton trajectory within a heterogeneous medium required for proton imaging. Phys Med Biol 2015;60(13):5071. https://doi.org/10.1088/0031-9155/60/13/5071.

[12] Schultze B, Witt M, Censor Y, Schubert K, Schulte R, Reich S, et al. Performance of hull-detection algorithms for proton computed tomography reconstruction. Contemp Mathe 2015;636:211–224. https://doi.org/10.1090/conm/636/12739.

[13] Schultze B, Karbasi P, Giacomelli V, Plautz T, Schübert KE, Schulte RW. Reconstructing highly accurate relative stopping powers in proton computed tomography. In: 2015 IEEE Nuclear Science Symposium and Medical Imaging Conference (NSS/MIC). IEE; 2015. p. 1–3. https://doi.org/10.1109/NSSMIC.2015.7582218.

[14] Agostinelli S, Allison J, Ka Amako, Apostolakis J, Araujo H, Arce P, et al. GEANT4—a simulation toolkit. Nuclear instruments and methods in physics research section A: Accelerators. Spectrometers, Detect Assoc Equip 2003;506(3):250–303. https://doi.org/10.1016/S0168-9002(03)01368-8.

[15] Ulrich-Pur F, Bergauer T, Burker A, Hatamikia S, Hirtl A, Irmler C, et al. Imaging with protons at MedAustron. Nucl Instrum Methods Phys Res Section A: Accelerat Spectrom Detect Assoc Equip 2020;978:164407. https://doi.org/10.1016/j.nima.2020.164407.

[16] Michalak G, Taasti V, Krauss B, Deisher A, Halaweish A, McCollough C. A comparison of relative proton stopping power measurements across patient size using dual-and single-energy CT. Acta Oncol 2017;56(11):1465–1471. https://doi.org/10.1080/0284186X.2017.1372625.

[17] The Phantom Laboratory. Catphan 600® Manual. 2021. https://www.phantomlab.com/catphan-600; accessed: 18.11.2021.

[18] Volz L, Piersimoni P, Bashkirov VA, Brons S, Collins-Fekete CA, Johnson RP, et al. The impact of secondary fragments on the image quality of helium ion imaging. Phys Med Biol 2018;63(19):195016.

[19] Ulrich-Pur F, Bergauer T, Burker A, Hirtl A, Irmler C, Kaser S, et al. Feasibility study of a proton CT system based on 4D-tracking and residual energy determination via time-of-flight. Phys Med Biol 2022;67(9):095005. https://doi.org/10.1088/1361-6560/ac628b.

[20] CIRS, Norfolk, VA, USA. Phantom Patient for Stereotactic End-to-End Verification. 2022. URL: https://www.cirsinc.com/products/radiation-therapy/phantom-patient-for-stereotactic-end-to-end-verification/; accessed: 23.03.2022.

[21] Santin G, Strul D, Lazaro D, Simon L, Krieguer M, Martins MV, et al. GATE: A Geant4-based simulation platform for PET and SPECT integrating movement and time management. IEEE Trans Nucl Sci 2003;50(5):1516–1521. https://doi.org/10.1109/TNS.2003.817974.

[22] Schneider W, Bortfeld T, Schlegel W. Correlation between CT numbers and tissue parameters needed for Monte Carlo simulations of clinical dose distributions. Phys Med Biol 2000;45(2):459. https://doi.org/10.1088/0031-9155/45/2/314.

[23] Schulte R, Penfold S, Tafas J, Schubert K. A maximum likelihood proton path formalism for application in proton computed tomography. Med Phys 2008;35(11):4849–4856. https://doi.org/10.1118/1.2986139.

[24] Sidky EY, Pan X. Image reconstruction in circular cone-beam computed tomography by constrained, total-variation minimization. Phys Med Biol 2008;53(17):4777. https://doi.org/10.1088/0031-9155/53/17/021.

[25] Berger M, Coursey J, Zucker M, Chang J. Stopping-power and range tables for electrons, protons, and helium ions, NIST Standard Reference Database 124. National Institute of Standards and Technology (NIST); 2017. https://doi.org/10.18434/T4NC7P.
[26] Collins-Fekete CA, Dikaios N, Royle G, Evans PM. Statistical limitations in proton imaging. Phys Med Biol 2020;65(8):085011. https://doi.org/10.1088/1361-6560/ab7972.
[27] Dickmann J, Wesp P, Rädler M, Rit S, Pankuch M, Johnson R, et al. Prediction of image noise contributions in proton computed tomography and comparison to measurements. Phys Med Biol 2019;64(14):145016. https://doi.org/10.1088/1361-6560/ab2474.
[28] Hatamikia S, Biguri A, Kronreif G, Figl M, Russ T, Kettenbach J, et al. Toward on-the-fly trajectory optimization for C-arm CBCT under strong kinematic constraints. Plos One 2021;16(2):e0245508. https://doi.org/10.1371/journal.pone.0245508.
[29] Soret M, Bacharach SL, Buvat I. Partial-volume effect in PET tumor imaging. J Nucl Med 2007;48(6):932–945. https://doi.org/10.2967/jnumed.106.035774.
[30] Dedes G, Dickmann J, Niepel K, Wesp P, Johnson RP, Pankuch M, et al. Experimental comparison of proton CT and dual energy x-ray CT for relative stopping power estimation in proton therapy. Phys Med Biol 2019;64(16):165002. https://doi.org/10.1088/1361-6560/ab2b72.
[31] Götz S, Dickmann J, Rit S, Krah N, Khellaf F, Schulte R, et al. Evaluation of the impact of a scanner prototype on proton CT and helium CT image quality and dose efficiency with Monte Carlo simulation. Phys Med Biol 2022;67(5):055003. https://doi.org/10.1088/1361-6560/ac4fa4.
[32] Rädler M, Landry G, Rit S, Schulte RW, Parodi K, Dedes G. Two-dimensional noise reconstruction in proton computed tomography using distance-driven filtered back-projection of simulated projections. Phys Med Biol 2018;63(21):215009. https://doi.org/10.1088/1361-6560/aae5c9.
[33] Liu Y, Ma J, Fan Y, Liang Z. Adaptive-weighted total variation minimization for sparse data toward low-dose x-ray computed tomography image reconstruction. Phys Med Biol 2012;57(23):7923. https://doi.org/10.1088/0031-9155/57/23/7923.
[34] Lohvithee M, Biguri A, Soleimani M. Parameter selection in limited data cone-beam CT reconstruction using edge-preserving total variation algorithms. Phys Med Biol 2017;62(24):9295. https://doi.org/10.1088/1361-6560/aa93d3.

Available online at: www.sciencedirect.com

ScienceDirect